European Journal of Mechanics B/Fluids 30 (2011) 552–564

Contents lists available at SciVerse ScienceDirect

European Journal of Mechanics B/Fluids

journal homepage: www.elsevier.com/locate/ejmflu

Numerical study of the hydrodynamics of regular waves breaking over a sloping beach

Pierre Lubin [a,*], Stéphane Glockner [a], Olivier Kimmoun [b], Hubert Branger [c]

[a] Université de Bordeaux, IPB, TREFLE UMR CNRS 8508, ENSCBP, 16 avenue Pey-Berland 33607 Pessac Cedex, France

[b] École Centrale de Marseille, Laboratoire de Recherche et Développement (LRD), Technopôle de Château-Gombert, 38 rue Joliot Curie, 13451 MARSEILLE Cedex 20, France

[c] Aix-Marseille Université, Institut de Recherche sur les Phénomènes Hors Équilibre (IRPHE), UMR CNRS 6594, Technopôle de Château-Gombert, 49 rue Joliot Curie, 13384 Marseille Cedex 13, France

ARTICLE INFO

Article history:
Available online 15 January 2011

Keywords:
Navier–Stokes
Large Eddy simulation
Two-phase flow
Breaking waves
Splash-up
Air entrainment

ABSTRACT

In the last three decades, great improvements have been made towards knowledge of the hydrodynamics and general processes occurring in the surf zone, widely affected by the breaking of the waves. Nevertheless, the turbulent flow structure is still very complicated to investigate. The aim of this work is to present and discuss the results obtained by simulating two-dimensional breaking waves by solving the Navier–Stokes equations, in air and water, coupled with a dynamic subgrid scale turbulence model (Large Eddy Simulation, LES). First, the ability of the numerical tool to capture the crucial features of this complicated turbulent two-phase flow is demonstrated. Numerical results are compared with experimental observations provided by Kimmoun and Branger (2007) [24]. Spilling/plunging breaking regular waves are considered. Generally, there is good agreement and the model provides a precise and efficient tool for the simulation of the flow field and wave transformations in the nearshore.

© 2011 Elsevier Masson SAS. All rights reserved.

1. Introduction

Simulating the air entrainment phenomenon generated by breaking waves remains a major challenge for modern CFD tools. Numerous problems motivated by fundamental research and applications, from environmental and coastal engineering sciences, require an accurate description of wave breaking. Highly complex hydrodynamic features are usually encountered in the surf zone: transition from irrotational flow motion to high frequency turbulence, interacting with large- and small-scale interface deformations, from overturning and breaking of the waves to complex fractioning and coalescence of bubbles and droplets. A broad range of relevant length and time scales is thus involved in this multiphase turbulent flow, making it extremely complicated to investigate both experimentally and numerically.

The general knowledge and understanding of turbulence generated by breaking waves have greatly been improved in the last three decades. Broken waves involve motions of different types and scales, including large-scale coherent vortical motions and small-scale turbulence [1]. Once waves break, a large amount of energy is released and turned into turbulence [2]. Nevertheless, a lot of work still has to be done, some aspects suffering from a lack of efficiency or unsolved limitations. It is widely accepted that such a complicated high-Reynolds number turbulent multiphase flow is inaccessible for Direct Numerical Simulations (DNS), Reynolds Averaged Navier–Stokes Equations (RANS) or Large Eddy Simulations (LES) therefore being effective alternatives.

Zhao and Tanimoto [3] first applied the LES method to breaking waves and showed very promising results compared with experimental measurements, considering a two-dimensional configuration. Then some numerical works proved the ability of the LES method [4–8] to deal with spilling, plunging, strongly plunging and spilling/plunging breakers. The authors provided a great improvement in the numerical methods allowing a description with a very promising accuracy for both the free surface and the general behavior of the turbulent flow structures. Major contributions gave interesting insights into the hydrodynamics under broken waves. Nevertheless, as all the cited authors stated, air entrainment was not taken into account, although it was widely identified as an important feature to be considered. Indeed, most numerical surf zone studies are based on single phase flow assumption, ignoring the air phase for the convenience of computation. Moreover, comparisons led to the conclusion that the poor description of air/water mixing was responsible for the discrepancies observed due to coarse mesh grid resolutions. Strong surface distortions, surface tension and air–water interactions were usually omitted. A generally good agreement was usually found, but some major differences were shown to occur when

* Corresponding author. Tel.: +33 0 540 003 307; fax: +33 0 540 006 668.
E-mail addresses: lubin@enscbp.fr (P. Lubin), glockner@enscbp.fr (S. Glockner), olivier.kimmoun@centrale-marseille.fr (O. Kimmoun), branger@irphe.univ-mrs.fr (H. Branger).

0997-7546/$ – see front matter © 2011 Elsevier Masson SAS. All rights reserved.
doi:10.1016/j.euromechflu.2011.01.001

phase-averaged velocity and turbulent quantities were examined in aerated regions. Indeed, the resolution was mainly chosen to provide acceptable computation times with a sufficient accuracy for the free surface description considering the macro structures. This often resulted in missing the correct breaking point, which is very sensitive to any imperfections in wave generation [8]. It was also found that the results of plunging breakers showed better agreement than spilling breakers compared to experimental measurements.

Many experimental works drew attention to the generation and the importance of air entrainment during the wave breaking process [9,10,1,11–13]. The velocity field under broken waves is characterized by the existence of very active turbulence associated with air entrainment, which is responsible for wave energy damping in the surf zone. Lin and Hwung [14] showed that the main mechanism driving the motion in the bubble region was the vortex system generated during the jet-splash cycles. Experiments proved that the eddies contained a large quantity of air bubbles which enhanced the upwelling of sediment. Chanson and Lee [15] measured the rate of energy dissipation to be increased with the bubble penetration depth. Huang et al. [16] recently presented experimental measurements of spilling breaking waves. Significant turbulent dissipation was shown to occur initially in the roller region at the frontal wave crest and then to spread to the entire crest region after the establishment of a turbulent bore. The small-scale interactions thus have important effects on large-scale behavior [17].

More recent numerical studies proved the importance of air entrainment for turbulence generation in numerical simulations of breaking waves. Christensen et al. [18] highlighted that since the mixture of air and water in the roller region had, on average, a smaller density than that of the water, the turbulence produced in the roller would have difficulties in penetrating the underlying fluid. Therefore, a large part of the production and dissipation took place in the roller before it was diffused downward, which explained the overestimation of the turbulence in the surf zone by numerical models so far. Moreover, the de-entrainment of air bubbles from the water after wave breaking may have released some wave energies into the air and may have contributed significantly to the wave energy dissipation process. Hieu and Tanimoto [19] improved their numerical model [5] showing better comparisons with experimental data concerning free surface elevations. The numerical results were also compared with those from Zhao et al. [6] and a higher accuracy was shown. They pointed out the major role of air entrainment and the necessity to take it into account to get accurate numerical results. Lubin et al. [20] discussed the results obtained from simulating three-dimensional plunging breaking waves by solving the Navier–Stokes equations, in air and water. The splash-up mechanism was carefully detailed and vortex generation and air entrainment processes were described. The behavior of the gas pockets was analyzed and its impact on energy dissipation was shown. Recently, Wang et al. [21,22] improved the numerical methods for describing the free surface, dedicated to breaking waves. Iafrati [23] numerically analyzed the role played by the breaking intensity on free surface dynamics, air entrainment and general hydrodynamics. Clear improvements were made to the general understanding of the complicated flow.

Kimmoun and Branger [24] recently experimented with surf zone breaking waves. Particle Image Velocimetry (PIV) experimental techniques were improved to be able to calculate velocities and void fractions in the aerated regions. Detailed pictures showed that a short spilling event occurred at the crest of the waves, before degenerating into a strongly plunging breaker. Numerical works usually showed better agreements when simulating plunging breaking waves than the spilling case compared with available experimental data. Fine mesh grid resolutions and appropriate numerical methods are required to accurately describe the length scales of the interface deformations experimentally measured (plunging jet, white foam, etc.).

Based on a previous numerical study, Lubin et al. [25] presented the results obtained for the LES of 2D and 3D regular waves shoaling and breaking over a sloping beach, compared with the experimental results of Kimmoun et al. [26]. A spilling/plunging breaking event was expected to occur according to the experimental measurements, but the numerical results showed discrepancies, due to the coarse mesh grid resolution. So, considering the new experimental results from Kimmoun and Branger [24] and the discrepancies highlighted by Lubin et al. [25], 2D numerical simulation of the phenomenon has been performed to show the ability of the numerical tool to finally capture the spilling initiation process and air entrainment during the early stage of the phenomenon. The effect of air has not been studied yet in detail in most of the cited two- and three-dimensional numerical studies found in the literature. Taking the mixture of air and water into account is crucial and still remains one of the challenges of future years. The aim of this paper is to simulate this unsteady two-phase wave breaking motion using a LES method to gain further understanding of the complicated features of the flow, including wave overturning, occurrence of splash-ups and air entrainment. The limitations in the description of the air entrainment will be highlighted and discussed. Great care will be taken to highlight the importance of the mesh grid size. The paper is organized as follows. In Section 2, we introduce the numerical model. The numerical wave generation procedure is detailed. Some preliminary numerical results and applications are provided to demonstrate the ability of the numerical tool to deal with breaking waves. We then provide, in Section 3, a discussion of the numerical results obtained by simulating regular waves breaking over a sloping beach. This section is devoted to the qualitative comparison of our numerical results with the experimental observations [24]. The case study is carefully described and boundary conditions are given. We aim to accurately describe the free surface behavior, as we will focus on capturing and describing the spilling phase experimented by Kimmoun and Branger [24]. Finally, in Section 4, a short critique of our numerical results is discussed. We then outline the perspectives and future works.

2. Description of the numerical model and validation

We solve the Navier–Stokes equations in air and water, coupled with a subgrid scale turbulence model (LES). The numerical tool is well suited to dealing with strong interface deformations occurring during wave breaking, for example, and with turbulence modeling in the presence of a free surface in a more general way. Solving the Navier–Stokes equations in an air/water configuration is still a real challenge, especially when dealing with strong interface deformations and tearing, turbulence and free surface interactions.

2.1. Governing equations

An incompressible multiphase phase flow between non-miscible fluids can be described by the Navier–Stokes equations in their multiphase form. In the single fluid formulation of the problem [27], a phase function C, or "color" function, is used to locate the different fluids standing $C = 0$ in the outer medium, $C = 1$ in the considered medium. Intermediate values of C indicate the proportion of the medium (water) in the control volume around each node of the mesh. The interface between two media is repaired by the discontinuity of C between 0 and 1. In practice, $C = 0.5$ is used to characterize this surface. The governing equations for the Large Eddy Simulation (LES) of an incompressible fluid flow are

classically derived by applying a convolution filter to the unsteady Navier–Stokes equations. The resulting set of equations reads (Eqs. (1)–(3)):

$$\nabla \cdot \mathbf{u} = 0 \tag{1}$$

$$\rho\left(\frac{\partial \mathbf{u}}{\partial t} + \mathbf{u}\cdot\nabla\mathbf{u}\right) = -\nabla p + \rho\mathbf{g} + \nabla\cdot(\mu+\mu_t)\left[\nabla\mathbf{u} + \nabla^T\mathbf{u}\right] + \mathbf{F} \tag{2}$$

and

$$\frac{\partial C}{\partial t} + \mathbf{u}\cdot\nabla C = 0 \tag{3}$$

where $\mathbf{u}$ is the velocity, C the phase function, t the time, p the pressure, $\mathbf{g}$ the gravity vector, ρ the density, μ the dynamic viscosity, μ_t the turbulent viscosity and $\mathbf{F}$ the surface tension volume force.

To deal with solid obstacles within the numerical domain, it is possible to use multi-bloc domains, but it is often much simpler to consider the numerical domain as a unique porous medium [28–30]. The permeability coefficient K defines the ability of a porous medium to let the fluids pass more or less freely through it. If this permeability coefficient is large ($K \to +\infty$), the medium is equivalent to a fluid. If it is zero, we can model an impermeable solid. A real porous medium is modeled with intermediate values of K. To take this coefficient K into account in our system of equations, we thus add an extra term in the right-hand side of the momentum equations (Eq. (2)), $-\frac{\mu}{K}\mathbf{u}$.

The magnitudes of the physical characteristics of the fluids depend on the local phase. They are defined according to C in a continuous manner as:

$$\begin{aligned}\rho &= C\rho_1 + (1-C)\rho_0\\ \mu &= C\mu_1 + (1-C)\mu_0\end{aligned} \tag{4}$$

where ρ_0, ρ_1, μ_0 and μ_1 are the densities and viscosities of fluid 0 and 1 respectively.

Based on the review of Lubin and Caltagirone [31], we find that the most widely used subgrid scale model is the Smagorinsky model. However, it has been proved to be much too dissipative [32]. In spite of its negative aspects, its simplicity is still widely appreciated. In Eq. (2), the turbulent viscosity μ_t is calculated with the Mixed Scale model [32], which has proved its accuracy for geophysical flows [33,34,20,35,36]. The model exhibits a triple dependency on the large and small structures of the resolved field as a function of the cut-off length. The eddy viscosity μ_t is calculated as follows (Eq. (5)):

$$\mu_t(\mathbf{x},t) = \rho C_M \overline{\Delta}^{1+\alpha}\left(|\overline{S}|\right)^{\frac{\alpha}{2}}\left(q_c^2(\mathbf{x},t)\right)^{\frac{1-\alpha}{2}} \tag{5}$$

where $\overline{S}$ is the resolved deformation rate tensor and $\overline{\Delta}$ is the cut-off length of the filter. C_M is the model constant chosen as $C_M = 0.06$, α is a parameter with a value that varies between 0 and 1. Generally, and in the following, α is taken to be equal to 0.5. The quantity q_c represents the kinetic energy of the test field extracted from the resolved velocity field through the application of a test filter associated to the cut-off lengthscale $\widetilde{\overline{\Delta}} > \overline{\Delta}$. We choose $\widetilde{\overline{\Delta}} = 2\overline{\Delta}$, because it is the value which is most used and seems to give the best results. This subgrid kinetic energy is assumed to be equal to the kinetic energy at cut-off q_c^2, evaluated in real space as (Eq. (6)):

$$q_c^2(\mathbf{x},t) = \frac{1}{2}\,\mathbf{u}(\mathbf{x},t)'\,\mathbf{u}(\mathbf{x},t)' \tag{6}$$

where the *test field* velocity ($\mathbf{u}'$) can be evaluated thanks to an explicit test filter applied to the resolved scales, noted $\widetilde{(.)}$. This explicit discrete filtering operation is a linear combination of the neighboring values [32,37]. This test field velocity represents the high frequency part of the resolved velocity field. The use of this model does not require a complementary wall model, as the Smagorinsky model does, because the eddy viscosity vanishes as the kinetic energy tends to zero at cut-off.

Model (Eqs. (1)–(4)) describes all the hydrodynamic and geometrical processes involved in the motion of multiphase media.

2.2. Numerical methods

Time discretization is implicit and the equations are discretized on a staggered grid by means of the finite volume method. A dual grid, or underlying grid [38], is used to gain improved accuracy for the interface description, the mesh grid size being divided by two in each direction for interface tracking. This technique also avoids the interpolations of the physical characteristics on the staggered grids, since the color function is defined on each point where viscosities and densities are needed.

The main difficulty concerning the numerical treatment of the Navier–Stokes equations (Eqs. (1) and (2)) is the coupling between pressure and velocity and the fulfillment of the incompressibility condition. Following the work of Fortin and Glowinski [39], the Navier–Stokes system is formulated as a velocity/pressure minimization–maximization problem requiring the computation of a saddle point ($\mathbf{u}$, $\mathbf{p}$) associated with the augmented Lagrangian of the problem. The pressure is considered as a Lagrange multiplier and the incompressibility constraint is introduced implicitly into the momentum equations (Eq. (2)). Then, the saddle-point ($\mathbf{u}$, $\mathbf{p}$) is computed using an iterative Uzawa algorithm [40]. Parameters of the augmented Lagrangian method are calculated automatically according to the fluids and flow characteristics following [41]. The space derivatives of the inertial term are discretized by a hybrid Upwind-Centered scheme [42] and the viscous term is approximated by a second order centered scheme. The MUMPS direct solver is used to solve the linear systems [43,44].

Interface tracking is achieved by a Volume Of Fluid method (VOF), which is able to handle interface reconnections without interface reconstruction. Lin and Liu [45] gave a complete overview and discussion of the different numerical techniques that have been used for interface tracking in numerical simulations of breaking waves. Given that Eq. (3) is hyperbolic and C is discontinuous, the explicit Total Variation Decreasing (TVD) Lax-Wendroff (LW) scheme of LeVeque [46] is used to directly solve the interface evolutions without the reconstruction of C. When the small scale structures of interface are large compared with the grid size, the LW-TVD method is accurate and involves controlled numerical diffusion across the interface on three grid points.

The numerical code has already been extensively verified and validated through numerous test cases including mesh refinement analysis [33,47,20,36]. The accuracy of the numerical schemes and the conservation laws of mass and energy in the computational domain have been accurately verified. For more details, the numerical methods have already been fully described in Lubin et al. [20].

2.3. Internal wave maker

Prior to the simulation of the laboratory tests, an effort has been made to implement and validate the procedure of regular and irregular wave generation developed by Lin and Liu [48]. The method consists of introducing an internal mass source function in the continuity equation (Eq. (1)) for a chosen group of cells defining the source region:

$$\nabla\cdot\mathbf{u} = S(x,y,t) \quad \text{in } \Omega \tag{7}$$

where $S(x,y,t)$ is calculated thanks to any chosen analytical wave solution.

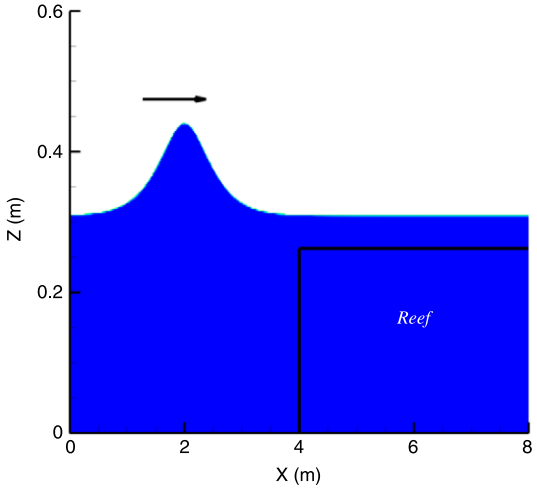

Fig. 1. Initial conditions for the propagation and the breaking of a solitary wave over a submerged rectangular reef. $t = 0$ s, $C > 0.5$.

2.4. Validation: a solitary wave propagating and breaking over a submerged obstacle

Lubin et al. [20] validated the numerical tool considering some dam-break and rising bubbles configurations. In this section, the propagation and the overturning of a stable solitary wave over a submerged reef, consisting of a rectangular step-like obstacle, is investigated (Fig. 1). The reference case is taken from the work presented by Yasuda et al. [49]. This test case shows the ability of our numerical model to simulate overturning waves accurately, as we will compare the wave profiles at breaking.

The mean water depth is $d = 0.31$ m and the height of the obstacle is $D = 0.263$ m. The initial amplitude and celerity are $H = 0.131$ m and $c = 2.072$ m s^{-1}, respectively. The incident solitary wave is initialized in the numerical domain and the crest of the wave is set at $x = 2$ m, the internal wave maker is not used in this test case. The reef face is located at $x = 4$ m. The velocity field and the free surface profile are initially calculated with the theoretical third-order solitary wave solution [50,51]. The numerical domain is 8 m long and 0.6 m high, discretized into 1200×200 nonuniform grids in the x-direction, with $\Delta x_{\min} \simeq 4 \times 10^{-3}$ m in the vicinity of the submerged obstacle. Uniform grid spacing $\Delta z_{\min} \simeq 3 \times 10^{-3}$ m is used. The solitary wave propagates towards the right side of the numerical domain.

Yasuda et al. [49] used a fully nonlinear potential theory model to study the internal velocity and acceleration fields and their relationship to breaker type. They verified the accuracy of their numerical model with some experimental data. Four capacitance wave gauges recorded the free surface elevations at different locations in the canal. The first gauge was placed upstream of the reef face to check the incident waveheight. The second gauge was located above the upstream corner of the reef. The last two gauges measured the free surface at 0.515 and 1.020 m away from the tip of the obstacle.

With respect to the positions of the three last gauges (referred to as P2, P3 and P4 by Yasuda et al. [49]), we plot our non-dimensional free surface elevations η/d versus non-dimensional time $t\sqrt{g/d}$, compared with the experimental values (Fig. 3). We can note that our numerical model gives very satisfactory results. The general trend is followed with reasonable accuracy, the relative errors being presented in Table 1.

We verify that our numerical model accurately reproduces the propagation and the interaction between the solitary wave and the obstacle. First, the wave propagates over a flat bottom without any change of form, as any stable solitary wave would do.

Table 1
Maximum non-dimensional free surface elevation values, η/d, recorded at the three considered locations. Numerical values are compared with the experimental measurements [49].

Gauges	Numerical	Experimental	Error (%)
P2	0.500	0.505	−1.0
P3	0.348	0.344	1.2
P4	0.358	0.354	1.1

As it reaches the neighborhood of the obstacle, the depth of water over the reef is abruptly reduced, which leads to the wave profile being dramatically transformed. The wave is then forced to reorganize itself, causing the fission phenomenon: when solitary waves propagate from deep water into shallower water, the incoming waves disintegrate into two or more solitons [52,53]. Fig. 2 present the incident wave separating into a solitary wave, going to the left, and a transmitted wave, which is about to break as it goes over the reef towards the right side of the domain. This aspect would have deserved more systematic investigation for validation, but it is not our concern in this paper.

As recorded by the gauge standing over the reef's upstream corner (Fig. 3), the free surface elevation rises from the initial non-dimensional value $\eta/d = 0.424$ to $\eta/d = 0.498$. The wave loses symmetry aspect and starts steepening till the front face of the crest becomes vertical (Fig. 4(a)). We then have a plunging breaking wave (Fig. 4(b)). A jet of liquid is about to be projected from the crest of the wave. It free-falls down forward in a characteristic overturning motion. It was observed that several gas pockets were entrapped.

In order to compare our results with the work of Yasuda et al. [49], we use the same non-dimensional values. Yasuda's reef face is located at $x/d = 32$, our reef being at $x/d \simeq 12.9$. So, we show in Fig. 4(a) and (b)) our free surface profiles translated to the same reference, with η/d the non-dimensional free surface elevation. Fig. 4(a) and (b) present the non-dimensional free surface profiles of the breaking wave at two different locations. At first glance, the comparisons are not to our advantage, but we voluntary zoomed the graphs, which enlarges the discrepancies. If we consider the abscissa of the vertical front face of the wave (Fig. 4(a)), the relative error between our numerical result and the experimental measurement is $\simeq -1.5\%$. At the instant of jet fall initiation (Fig. 4(b)), if we again consider the abscissa of the vertical face of the wave, under the overhanging jet, the relative error between the numerical result and the experimental measurement is $\simeq -1.2\%$. The numerical and experimental jets of water are approximately of the same length. However, we can observe that the computed jet looks "thicker" than the experimental one. This tendency is generally observed when using VOF methods for simulating breaking waves [54,33,21].

Unfortunately, Yasuda et al. [49] presented no experimental pictures giving information about the abscissa of the jet impact or the splash-up behavior. However, our numerical results fit very well with the published results of Yasuda et al. [49] considering the wave breaking initiation phenomenon. The ability of the numerical tool to predict accurately the breaking point initiation is thus proved.

3. Large eddy simulations of breaking waves

Based on the numerical methods detailed in Section 2, Lubin et al. [25] presented the results obtained for the LES of regular 2D and 3D waves shoaling and breaking over a sloping beach, compared with the experimental results from Kimmoun et al. [26]. The main observed differences were that the first short spilling event was missed and the dislocation of the gas pockets into small bubbles could not be simulated, even though, in the numerical

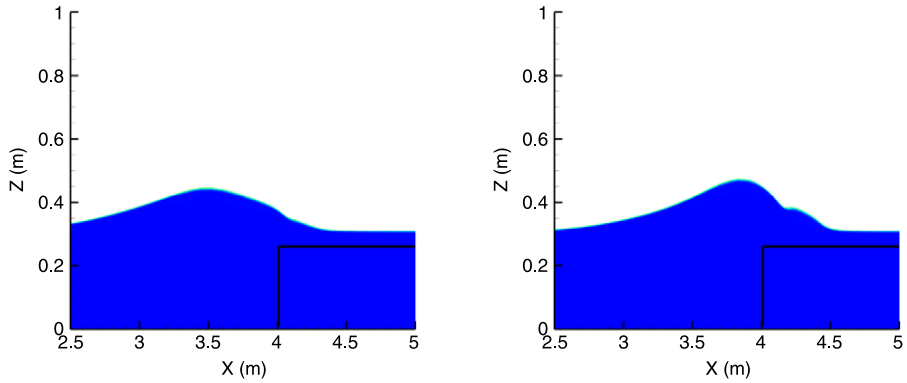

(a) $t = 0.7$ s. (b) $t = 0.91$ s.

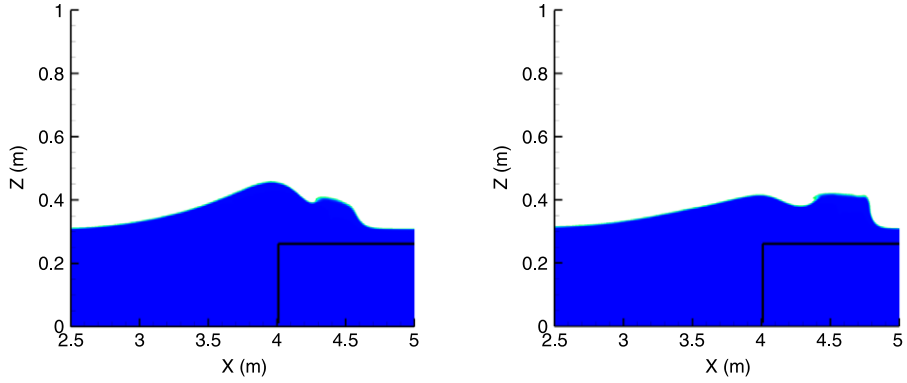

(c) $t = 1.1$ s. (d) $t = 1.2$ s.

Fig. 2. Solitary wave propagating over the submerged reef: initiation of the fission of the wave. The black line represents the reef profile. $C > 0.5$.

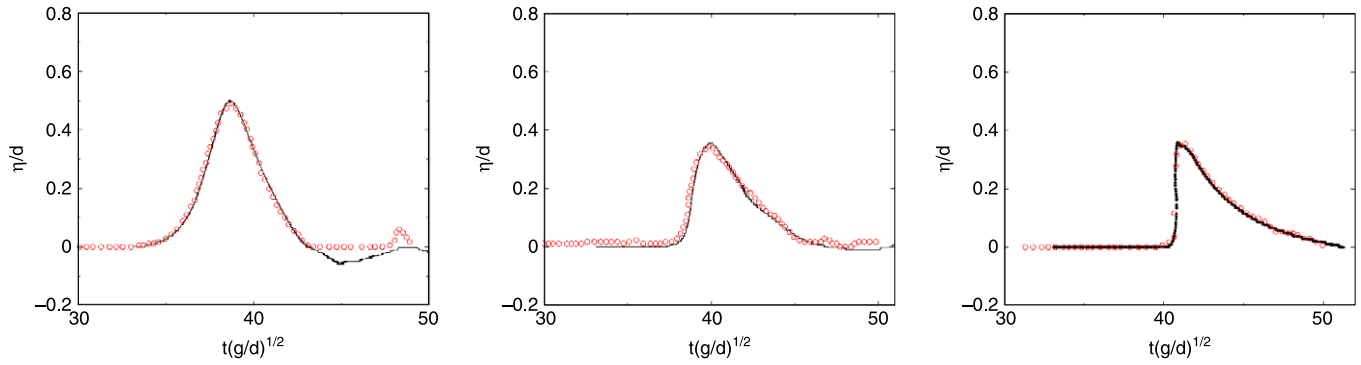

(a) P2. (b) P3. (c) P4.

Fig. 3. Comparisons of the non-dimensional free surface elevations, η/d, plotted versus the non-dimensional time, $t\sqrt{g/d}$, recorded at each location P2, P3 and P4. Black line: present numerical results; red ○: experimental results [49].

results, the gas pockets corresponded to some air–water mixing zones observed in the experimental pictures. In order to overcome the observed discrepancies, mainly due to the coarse mesh grid resolution, new numerical simulation was performed considering the new experimental study from Kimmoun and Branger [24]. The mesh grid distribution was improved to be able to capture the spilling phase.

3.1. Description of the experimental configuration

The experiments were performed in the École Centrale wave tank in Marseille. The glass-windowed tank is 17 m long and 0.65 m wide. The water depth was set at $d = 0.705$ m. The 1/15 sloping beach was about 13 m long, starting at about 4 m from the wavemaker. The length of the surf zone was about 3 m. Camera PIV measurements were made in fourteen different locations from the incipient breaking location up to the swash zone. Fifth order Stokes waves were generated, corresponding to the analytical solution developed by Fenton [55]. The wave period was $T = 1.275$ s and wave amplitude before the sloping beach was $a \simeq 0.057$ m. The wavelength was $L \simeq 2.4$ m and the measured height at breaking was $H_b = 0.14$ m. The waves are observed to start breaking about 2.50 m away from the shoreline, or 12.275 m away from the wavemaker.

A sketch of a wave breaking event is displayed by Kimmoun and Branger [24]. The wave starts breaking showing a brief spilling phase, the white cap was observed to be about 1-mm thick. Then a jet of liquid is rapidly ejected from the wave crest and the overturning wave front curls forward. A first splash-up is generated when the jet of liquid hits the front face of the wave.

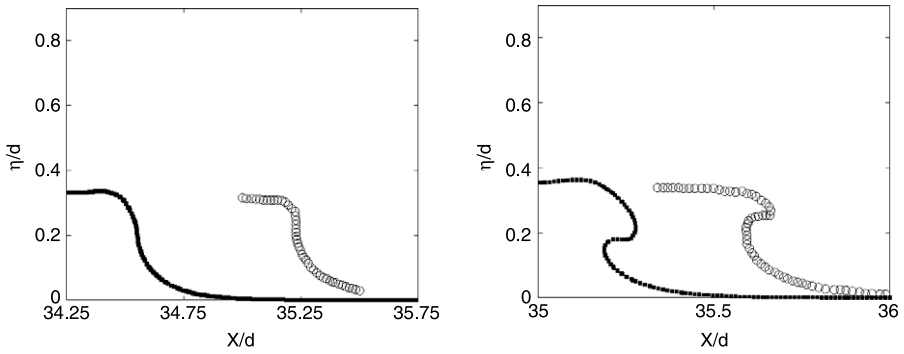

(a) Breaking point. (b) Jet fall initiation.

Fig. 4. Comparison of the free surface profiles (a) prior to the jet ejection and (b) at jet initiation. Black ■: present LES ($C = 0.5$); black ○: experimental results [49]. The variables indicated on both axis are those shown in Fig. 4 by Yasuda et al. [49].

We can then see a large amount of air entrained with foam and bubbles. Some other splash-ups are then generated. A roller propagates towards the shoreline, with a great air–water mixing area. It can be seen that the bubbles are generated in the upper part of the water column, and advected towards the bottom with a slight slanting axis. The volume of the entrained bubbles decreases gradually till the wave crosses the shoreline and runs up before coming back. This is in agreement with the general description of Peregrine [56], for example. More details of the experiments are given by Kimmoun and Branger [24].

3.2. Initial and boundary conditions

The computational domain is 15 m long and 1 m high (Fig. 5). The sloping beach starts at $x = 3.5$ m, the source function being located at $x_S = 3.5$ m and $z_S = 0.3675$ m. The center of the source region is at $d/2$, right above the toe of the sloping beach to save computation time. The numerical beach is considered as an impermeable solid obstacle, the permeability coefficient K being initialized at zero (Eq. (2)).

522 000 mesh grid points are used to discretize the numerical domain, with nonuniform grids in both directions ($\Delta x_{\min} \simeq 1 \times 10^{-3}$ m and $\Delta z_{\min} \simeq 2.5 \times 10^{-3}$ m). These values have to be divided by two, in both directions, for the free surface description thanks to the dual grid. Two-phase flow simulations and turbulence modeling require fine mesh cells to be very accurate, even if LES is supposed to save some mesh grid points. Moreover, when simulating two-phase flows, the interface can become smaller than the mesh grid size (droplets or bubbles). These small inclusions are thus "lost" and their contribution to the flow can lead to an incorrect description of the flow. In our study, the major physical parameters leading the choice of our mesh grid distribution are the length scales of the free surface deformations, especially the overturning jet and the entrained gas pockets.

The time step is chosen to ensure a Courant–Friedrichs–Levy condition less than 1, necessary for the explicit advection of the free surface. The calculation is made with the densities and the viscosities of air and water ($\rho_a = 1.1768$ kg m^{-3} and $\rho_w = 1000$ kg m^{-3}, $\mu_a = 1.85 \times 10^{-5}$ kg m^{-1} s^{-1} and $\mu_w = 1 \times 10^{-3}$ kg m^{-1} s^{-1}). Table 2 presents the former and new physical and numerical parameters, used in the successive studies.

We adapted Fenton's [55] analytical developments for the fifth-order Stokes wave theory, corresponding to the experimental conditions, to the source function method (Eq. (7)):

$$S(x, y, t) = \sum_i \sum_j \frac{2c}{Ak} B_{ij} \epsilon^i \cos i \left(\frac{\pi}{2} - \sigma t - p_s \right) \tag{8}$$

where A is the area of the source region. c, k and σ are the celerity, wave number and angular frequency respectively. $\epsilon = \frac{kH}{2}$ is the wave steepness and B_{ij} are dimensionless coefficients. The detailed expressions for the dispersion relationship, wave celerity and B_{ij} coefficients are given by Fenton [55], Sobey et al. [57] or Fenton and McKee [58]. p_s is the phase shift calculated to have $S(x, y, 0) = 0$. The source region is 0.06 m wide and 0.0735 m high. The area and the location of the source function have been designed applying the rules described by Lin and Liu [48]. The height of the source region is recommended to be in the range of $1/10 - 1/2$ of water depth, while the width of the source region is suggested to be less than 5% of the wavelength. The distance between the center of the source region and the still water level is advised to be in the range of $1/3 - 1/2$ of the water depth. The method has been extensively verified and validated compared with analytical profiles to ensure accurate wave generation.

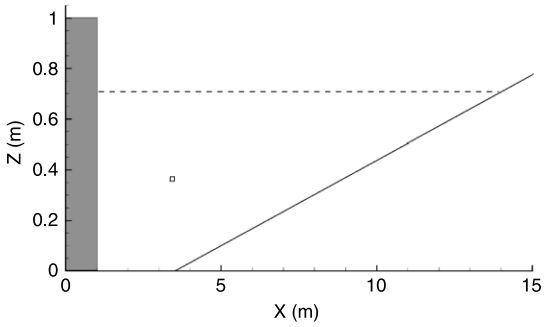

Fig. 5. Numerical domain configuration. The small rectangular box is the wave generator, located right above the toe of the sloping beach. The dashed line shows the initial water depth. The gray box on the left side of the numerical domain is a sponge layer. The slanted line shows the sloping beach.

Table 2
Physical and numerical parameters used in the successive studies. The mesh grid sizes have been divided by two considering the dual grid used for the interface capture (see Section 2.2).

Experimental studies	Kimmoun et al. [26]	Kimmoun and Branger [24]
d (m)	0.735	0.705
T (s)	1.3	1.275
a (m)	0.07	0.057
L (m)	2.5	2.4
H_b (m)	0.137	0.14
x_b (m)	2.65	2.5
Numerical comparisons	**Lubin et al. [25]**	**Present study**
Sizes of domains	20 m × 1.2 m	15 m × 1 m
Mesh grid points	520 000	522 000
$\Delta x_{\min}$ (m)	5×10^{-3} m	$\simeq 5 \times 10^{-4}$ m
$\Delta z_{\min}$ (m)	$\simeq 1.25 \times 10^{-3}$ m	$\simeq 1.25 \times 10^{-3}$ m

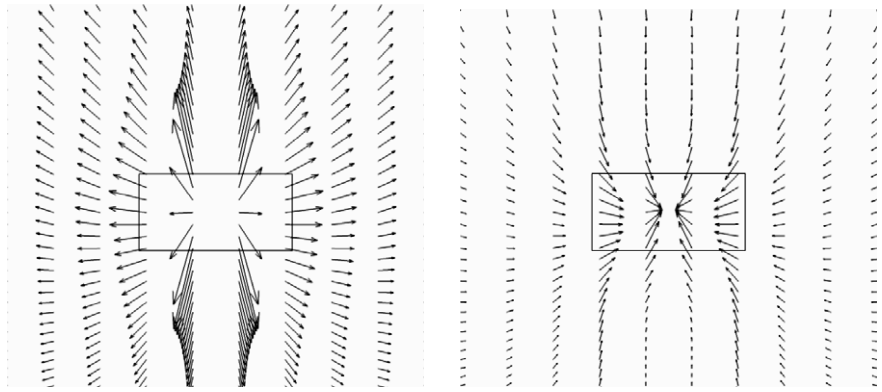

(a) $S(x, z, t) > 0$. (b) $S(x, z, t) < 0$.

Fig. 6. Velocity fields generated by the presence of the source function.

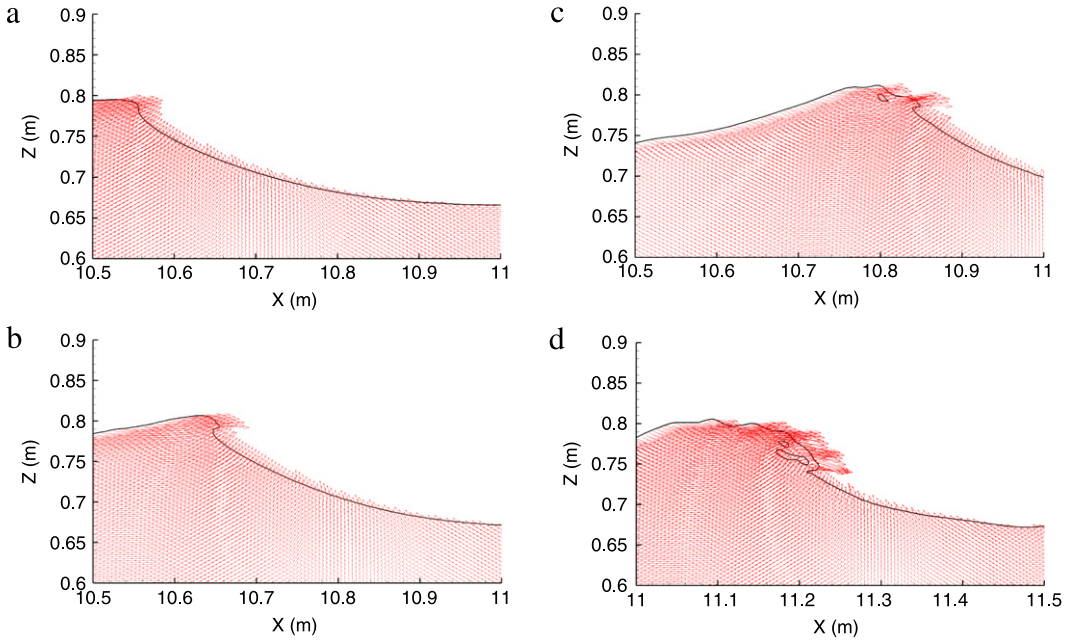

Fig. 7. Breaking wave evolution with velocity field in water. Only one vector over two is shown. Tenth breaking wave spilling phase initiation and jet ejection. The free surface profile corresponds to $C = 0.5$.

At the beginning of the numerical simulation, the water is at rest, and, as the time increments, the source function is calculated to generate the regular waves. In Fig. 6, we show the velocity field around the source function, acting like a pump. Two trains of surface gravity waves are thus generated, as the free surface responds to a pressure increment defined within the source region cells.

The two wave trains propagate in opposite directions towards both ends of the numerical domain. The Neumann boundary condition is thus set at the left side of the numerical domain to let the outgoing wave exit the numerical domain. In order to ensure that no numerical reflection occurs at the left side of the numerical domain, a sponge layer is set in addition to the Neumann boundary condition. It consists in a region where the permeability coefficient K is chosen such that the outgoing wave train is properly attenuated before reaching the open boundary.

As detailed by Hieu and Tanimoto [19], the source function is gradually intensified during the first four wave periods to ensure a stable regular wave train generation. So the first four generated waves are smaller than the experimental wave height. The small waves are observed to reach the shore and run-up along the beach without breaking. After four wave periods, the simulated waves reach the desired amplitude and the sixth wave starts breaking as a plunging breaker at $x_b \simeq 108$ cm away from the shoreline. The breaking point then moves offshore, as the next two waves overturn as strong plunging breakers again. The first spilling event is observed as the ninth wave break. Fifteen breaking waves were simulated. Only instantaneous quantities are presented and discussed.

3.3. Results and discussion

Experimentally, the white cap was about 1-mm thick as shown by Kimmoun and Branger [24] in their Fig. 4 — windows 2 and 3. So, numerically, the mesh grid refinement and the distribution were chosen to be able to capture this feature. In Figs. 7, 9 and 10, we present the free surface evolution with the numerical velocity field in the water, corresponding to the 10th breaking wave. In Fig. 11, we present some snapshots of the free surface evolution with the numerical velocity fields in both media, air and water, corresponding to the same 10th breaking wave.

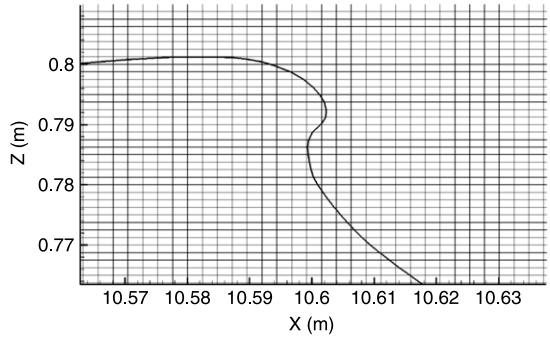

Fig. 8. Jet ejection at the crest of the breaking wave for initiation of the spilling phase. Mesh grid is shown with the free surface profile corresponding to $C = 0.5$. Dual grid not shown here.

3.3.1. General flow description

Spilling breakers are observed to start as a small zone of bubbles and droplets on the forward side of the crest [59,24]. This small region then grows by spreading downslope, most of the forward face becoming a turbulent flow region. Duncan [59] reported that, for the long wavelengths considered here, spilling breakers can be initiated by a small jet at the crest of the wave, creating a small turbulent patch of fluid well above the mean water level. Fig. 7 present the initiation of the spilling phase. Once the front face of the crest steepens and becomes vertical (Fig. 7(a)), a thin jet of water is indeed observed to be projected (Fig. 7(b)). In our numerical results, the spilling phase then starts as a very weak plunging breaking wave, with a small tongue of water thrown from the crest developing and free-falling down forward into a characteristic overturning motion. This is in accordance with reports from Duncan [59] and Kimmoun and Branger [24]. Miller [9] also presented pictures showing a spilling breaking wave starting with a 5-mm thick impinging jet at the crest of the wave. Once the jet is ejected from the wave crest and plunges down, it hits the water at the plunge point, located very near the crest of the wave. The plunging jet closes over a small gas pocket (Fig. 7(c)). The resulting splash is directed down the wave leading to a spilling breaker (Fig. 7(d)), where white foam, consisting of a turbulent air/water mixing, should appear at the wave crest and spill down the front face of the propagating wave [59,24].

However, compared with the 1-mm thick layer of foam initiating the experimental spilling wave from Kimmoun and Branger [24], we find that the gas pockets entrapped are about 5-mm thick. Fig. 8 presents the jet appearing at the wave crest and the mesh grid density used to capture the generation of the jet. The jet is clearly very small, about 1-cm thick, but it is probably thicker than experimentally. This is probably due to the same tendency detailed in Section 2.4, where the plunging jet was also thicker than experimentally measured.

Then, the spilling breaker transitions into a strong plunging breaker (Fig. 9(a)). A jet is ejected further towards the lower part of the face of the steepening wave. The plunging breaking wave is then responsible for the generation of larger jet-splash cycles, this, in turn, being responsible for the generation of a sequence of large-scale coherent vortices (Fig. 9(b)).

A high velocity region is located at the breaking crest of the wave. High splash-ups are rising, with high velocities directed upward, in the wave propagation direction, which generates counter- and co-rotative vortices (Fig. 9(b) and (c)), as observed by Bonmarin [60], Miller [9] or Sakaï et al. [61]. This process is observed to repeat, each successive splash-up being weaker than the preceding one. Large volumes of air and water are put into rotation, the successive rebounds causing more entrainment of air and energy dissipation. Miller [9] indicated the formation of many air bubbles during the jet-splash cycles which illustrated

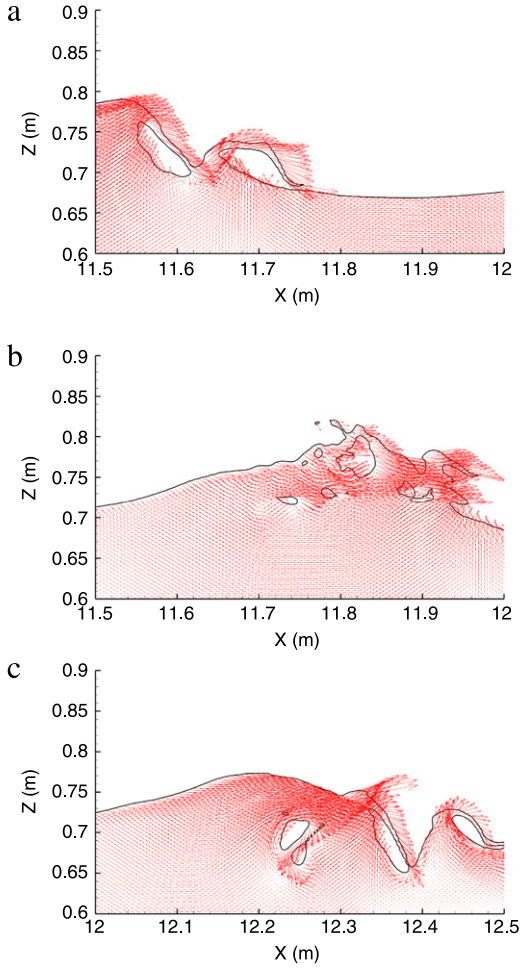

Fig. 9. Wave in the process of breaking with velocity field in water. Only one vector over two is shown. Tenth breaking wave transition to strong plunging breaker with splash-ups generation and air entrainment (continuation of Fig. 7). The free surface profile corresponds to $C = 0.5$.

that the vortices in plunging breakers significantly affect bottom flow. Large spinning gas pockets are observed in our numerical results, dissipating wave energy. Most of the rotating structures are entrained to the bottom before rising again to the surface. And once the wave moves into a bore propagating towards the shoreline (Fig. 10(a)–(c)), we have very similar results for the free surface description detailed by Kimmoun and Branger [24]. High velocities are located near the free surface, due the jet-splash cycles, during the bore propagation. The free surface is distorted and very dynamic. The bore running up the beach at some point meets the flow running down from the previous broken wave.

Nevertheless, discrepancies again appear. Experimentally, air cavities are observed to be quickly fragmented into large plumes of bubbles. The dislocation of the gas pockets into small bubbles cannot be simulated, even if, in the numerical results, the gas pockets correspond to some air–water mixing zones observed in the experimental pictures. This is due to the mesh grid resolution, which is still too coarse to be able to capture this flow feature. Indeed, the order of magnitude of bubble radii is usually 10^{-4} m [62], whereas our mesh grid resolution is $\Delta x_{\min} \simeq 5 \times 10^{-4}$ m and $\Delta z_{\min} \simeq 1.25 \times 10^{-3}$ m thanks to the dual grid. We are able to track the largest gas pockets and bubbles greater than 1 mm, as illustrated in the figures presented in this paper, where a large variety of inclusion length scales can be seen. Turbulence is associated with air entrainment, which is responsible for wave energy damping in the surf zone. In the experiments, it appears

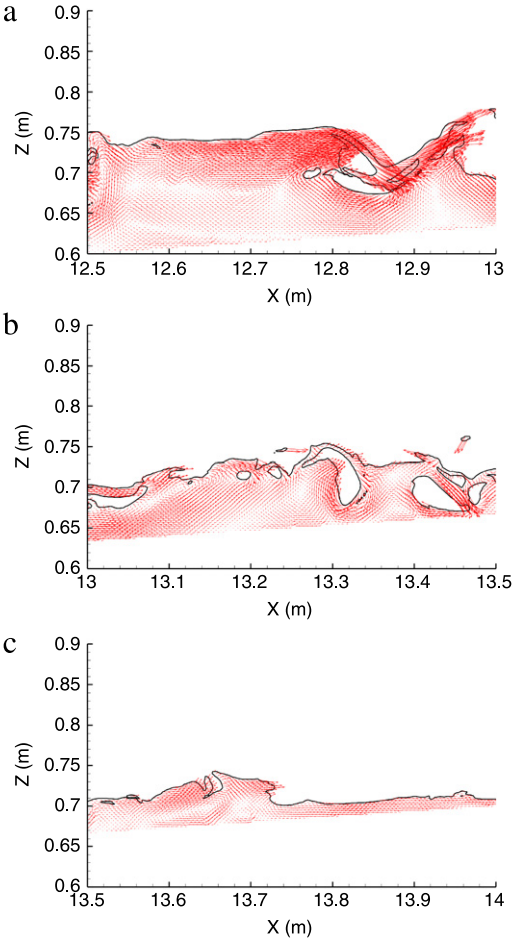

Fig. 10. Wave in the process of breaking with velocity field in water. Only one vector over two is shown. Tenth breaking wave transition to strong plunging breaker and run-up of the bore (continuation of Figs. 7 and 9). The free surface profile corresponds to $C = 0.5$.

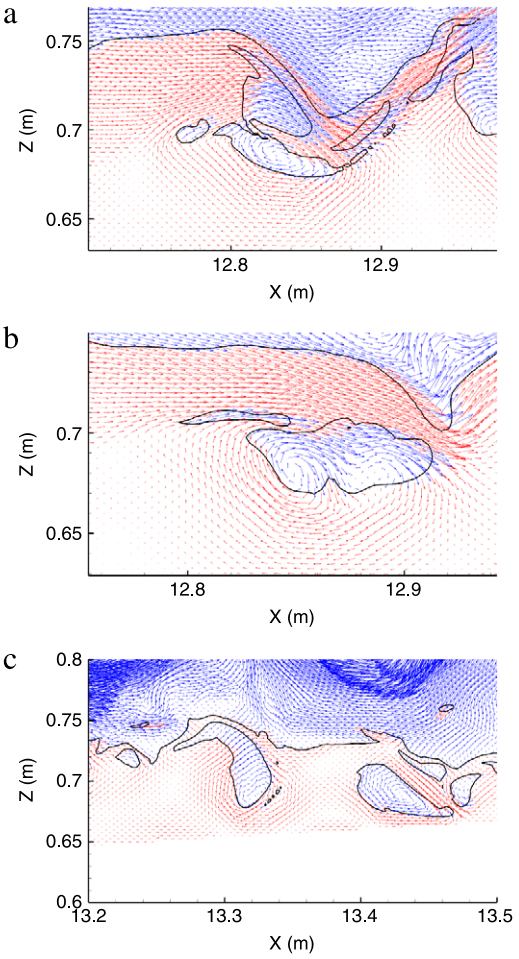

Fig. 11. Snapshots of the wave in the process of breaking with velocity field in air and water. Only one vector over two is shown. Tenth breaking wave transition to strong plunging breaker with rotating and dislocating gas pockets. The free surface profile corresponds to $C = 0.5$.

that the entrained air bubbles are contained mostly in the large structures and diffused towards the bottom due to the eddies. The rate of energy dissipation is increased with the bubble penetration depth and strong vertical motion is induced by the rising air bubbles. These mechanisms are mostly 3D, which cannot be taken into account in a 2D numerical simulation. Moreover, numerical diffusion due to the LW-TVD method [46] must also be responsible for the discrepancies. The free surface is diffused over three mesh grid cells, so any small inclusions (droplets or bubbles) are described less precisely.

We can also see strong flow dynamics in the air. We can see that the spilling phase occurs in quiet air dynamics and then meets air agitation generated by the previous breaking waves. A large amount of air is affected by the violence of the plunging breaking event. Fig. 11 present some snapshots of gas pockets entrapped at various stages of the breaking of the tenth wave. Rotating and fractioning air pockets can be clearly seen. A large range of inclusions can be described by the numerical simulation, interacting with complex free surface behavior and chaotic hydrodynamics.

3.3.2. Quantitative comparisons

Table 3 compares the locations of the spilling breaking point, the plunging occurrence and the first splash-up generation, from the numerical and experimental results. The shoreline is located at $x_S = 14.075$ m (see Fig. 5). The wave height at breaking is $H_b = 13$ cm, compared with the experimental value $H_b = 14$ cm.

Table 3
Experimental and numerical values for the approximate locations of the beginning of the main events: beginning of spilling breaking *sb*, beginning of plunging breaking *pb* and beginning of first splash-up *s*1 (see Figs. 12 and 13 from Kimmoun and Branger [24]). Distances are given from the shore.

	Experimental study	Numerical simulation
H_b (cm)	14	13
sb (cm)	$\simeq -250$	$\simeq -358$
pb (cm)	$\simeq -210$	$\simeq -280$
*s*1 (cm)	$\simeq -170$	$\simeq -250$

The numerical breaking point is located at $x_b \simeq 358$ cm away from the shoreline, compared with the experimental value $x_b \simeq 250$ cm. The occurrence of breaking was numerically detected when the horizontal velocity component reached a magnitude higher than the wave celerity, matching with a vertical topography of the front face of the wave (see Fig. 9(a)). The sequence of the main events can be qualitatively well described by the numerical tool, as the same distance separates approximately each event.

Fig. 12 compares the numerical and experimental results for the crest-envelopes (locations of the wave maxima) and the trough-envelopes (locations of the wave minima). Arrows indicate the locations of the main events (beginning of breaking, beginning of plunging and beginning of the first splash-up). The general trend of the flow is found to be qualitatively well described.

Fig. 13 compares the numerical and experimental wave profiles and velocity fields for the main events. Despite the discrepancies

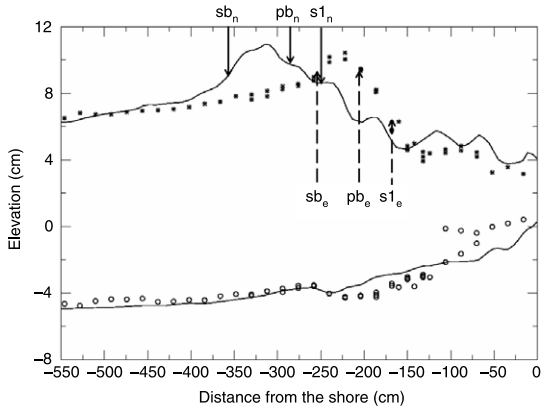

Fig. 12. Comparison of the space evolution of the maximum and minimum water levels near the shoreline. Symbols: experimental measurements (stars: wave crest; circles: wave trough). Solid lines: numerical results. The occurrence of the main events are indicated, for the numerical (sb_n, pb_n and $s1_n$) and experimental results (sb_e, pb_e and $s1_e$).

in the abcissae, a general agreement can be seen in the velocity magnitudes and free surface description. Fig. 14 presents the numerical and experimental wave profiles when the broken wave runs-up along the beach. Air entrainment can be seen in the experimental pictures with the gray areas. As already mentioned, the gas pockets observed in the numerical pictures correspond to some air–water mixing zones presented in the experimental pictures, but the coarse mesh grid size does not allow the dislocation of the pockets into bubbles. Splash-ups cycles are well described, with horizontal eddies generation [20,24].

The general trend of the flow dynamics is found to be correctly simulated.

3.3.3. General discussion

So, we slightly underpredict the wave height at breaking and waves break earlier than experimentally observed. It has been observed that a steady breaking point was not yet reached. Indeed, some variations occurred in the last breaking waves giving x_b varying by ± 60 cm. This is consistent with the experimental observations, the breaking point varying by ± 30 cm around the average value. For each experimental run, the 128 first wave cycles were dedicated to reaching a statistical quasi-stationary sea-state before starting data acquisition [24]. Image acquisition duration was set to 128 wave periods (wave-cycles 129–256).

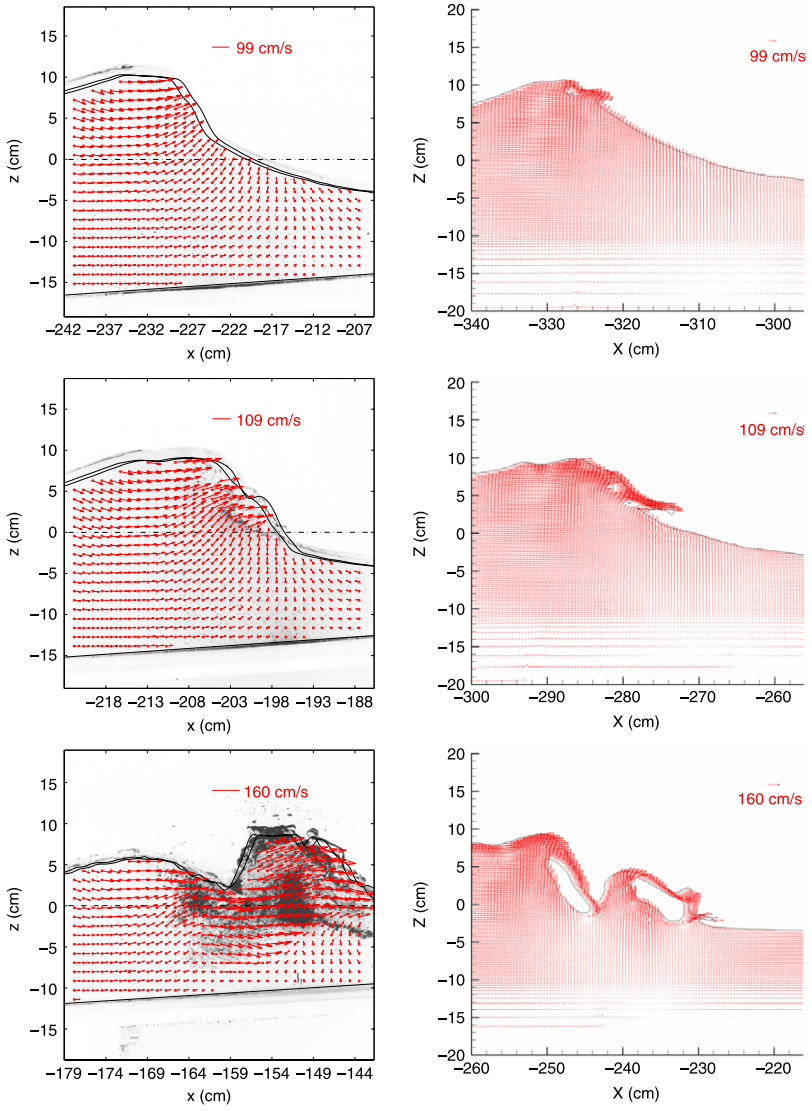

Fig. 13. Comparison for the main breaking events (spilling *sb*, plunging *pb* and first splash-up *s*1). Right column: numerical results; left column: experiments.

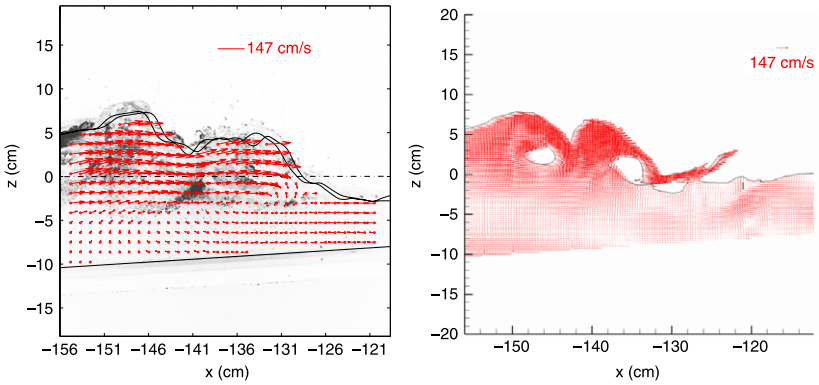

Fig. 14. Comparison for the broken wave running-up the beach. Right column: numerical results; left column: experiments.

Experimentally, the ten first breaking waves were observed to differ from one another.

This remark raises an issue that should be addressed: how many wave cycles should be simulated to be compared with experimental results? For example, Ting and Kirby [63–65] indicated that waves were generated for a minimum of 20 mn before data were taken, which gives 250–600 periodic waves (considering plunging and spilling breakers, respectively). Lin and Liu [66] simulated about ten periodic waves considering spilling breakers [64]. The computed results for mean velocities and free surface profiles indicated that the waves computed in the surf zone have nearly, but not completely, reached the quasi-steady state, i.e. there was very a small difference between two successive wave cycles. Lin and Liu [67] confirmed that, with the improvement of the wave generation mechanism and absorbing boundary conditions, the RANS models could run a long time until the waves reached the quasi-steady state, during which both the mean water level and time-averaged mean flow field could be accurately computed. However, the turbulence closure models did not give completely satisfactory results for turbulence simulation in the surf zone, the errors ranging from 25% to 100% for the turbulence calculation in the spilling breaker. With LES, Christensen [8] computed the experimental configurations of Ting and Kirby [64,65], calculating average quantities over the last five wave periods considering 16–20 wave periods (plunging and spilling breakers, respectively). Wang et al. [22] simulated up to ten spilling waves [64], calculating average quantities over the last two wave periods. Hieu and Tanimoto [19] set a computation time of 50 s, checking that time profiles of free surface elevations were almost stable after 30 s. When compared with to experimental results [64,65], better agreement was shown for plunging breakers. Nadoaka et al. [68] discussed the fact that the breaking point is sensitive to any imperfection in wave generation or to the effect of the previous broken wave. Therefore, the different wave generation procedures used between experiments and numerical simulations may also have contributed to the discrepancies observed in the comparisons presented in this paper. High order moments, such as skewness and flatness of the velocity signal, probably have to be estimated to check that steady state is reached in numerical simulations, to ensure accurate turbulent quantities.

It has therefore been proved that our simulation of fifteen wave periods was insufficient to get a stable and accurate breaking point. Indeed, we observed that the last three waves broke as plunging breakers. So more wave periods would be needed to clearly address this issue. Thus, we did not calculate average quantities, considering the expected discrepancies which could have resulted from the comparisons. Considering these simulations as a validation step, our numerical model gives very satisfactory and encouraging results for this 2D configuration.

4. Conclusions and perspectives

We focused on describing the spilling phase of the experiments detailed by Kimmoun and Branger [24]. The numerical results presented in this paper concern instantaneous quantities, simulating 2D regular waves breaking over a sloping beach. Our model was found to be reliable to describe correctly the complicated two-phase flow interactions that happen when waves break. The breaking process, in terms of wave overturning and splash-up occurrence, is in accordance with the general observations given in the literature. Air entrainment is described, which is important as it plays a great role in the energy dissipation process. The utility of the numerical approach is to provide a complete and accurate description of free surface and velocity evolutions in both air and water media during the breaking of the waves, which must lead to the understanding of the generation processes of energy dissipation and turbulent flow structures. Nevertheless, wave breaking is a 3D two-phase turbulent problem, so the 2D numerical results presented here consisted in a first attempt.

A major limitation of our numerical methods has been illustrated in the results presented in this paper. The accuracy of the whole physical process description is closely linked to the mesh grid size. Although LES allows the use of coarser mesh grids to simulate turbulent flows, on the condition that an appropriate subgrid model is implemented, an accurate free surface description requires fine mesh grids. LES of breaking waves involve large numerical domains, to include the generation of regular waves propagating towards sloping beaches, and fine mesh grid resolutions to be able to describe a large variety of physical processes (overturning jet, air entrainment, gas pocket dislocations and coalescences). A long CPU time for the calculations is also required to simulate a sufficient number of wave periods to reach a steady state in the surf zone to perform correct averaging over time. Parallel computing will enhance access to a better level of description of the turbulent behavior of the entrained and rising air bubbles, providing refined mesh grids are used to ensure an accurate free surface description [36].

With mesh refinement and 3D simulations, we could expect a better description of the air entrainment and energy dissipation. Considering the difficulty to capture all the small bubbles and droplets encountered in the wave breaking problem, these small interface structures can also be considered as subgrid interfaces. Mimicking the LES approach for turbulence, an appropriate model of inclusions smaller than the mesh grid size could then be proposed [69].

Acknowledgements

The authors wish to thank the Aquitaine Regional Council for the financial support towards a 256-processor cluster investment,

located in the TREFLE laboratory. This work was granted access to the HPC resources of CINES under allocation 2009-c2009026104 made by GENCI (Grand Equipement National de Calcul Intensif). The authors would like to acknowledge the financial and scientific support of the French INSU - CNRS (Institut National des Sciences de l'Univers - Centre National de la Recherche Scientifique) program IDAO (“Interactions et Dynamique de l'Atmosphère et de l'Océan”). This work was carried out under the project “Wave-induced circulation in the surf zone” coordinated by Dr. Hervé Michallet (LEGI - Grenoble).

References

[1] J.A. Battjes, Surf-zone dynamics, Annu. Rev. Fluid Mech. 20 (1988) 257–293.
[2] I.A. Svendsen, U. Putrevu, Surf-zone hydrodynamics, in: Advances in Coastal and Ocean Eng., vol. 2, World Scientific, 1996, pp. 1–78.
[3] Q. Zhao, K. Tanimoto, Numerical simulation of breaking waves by large eddy simulation and vof method, in: Proc. of the 26th Int. Conf. Coastal Eng., Vol. 1, ASCE, 1998, pp. 892–905.
[4] E.D. Christensen, R. Deigaard, Large eddy simulation of breaking waves, Coastal Eng. 42 (2001) 53–86.
[5] P.D. Hieu, K. Tanimoto, V.T. Ca, Numerical simulation of breaking waves using a two-phase flow model, Appl. Math. Model. 28 (11) (2004) 983–1005.
[6] Q. Zhao, S. Armfield, K. Tanimoto, Numerical simulation of breaking waves by multi-scale turbulence model, Coastal Eng. 51 (2004) 53–80.
[7] Y. Watanabe, H. Saeki, R.J. Hosking, Three-dimensional vortex structures under breaking waves, J. Fluid Mech. 545 (2005) 291–328.
[8] E.D. Christensen, Large eddy simulation of spilling and plunging breakers, Coastal Eng. 53 (2006) 463–485.
[9] R.L. Miller, Role of vortices in surf zone predictions: sedimentation and wave forces, in: R.A. Davis, R.L. Ethington (Eds.), Soc. Econ. Paleontol. Mineral. Spec. Publ., 1976, pp. 92–114 (Chapter 24) doi:10.2110/pec.76.24.0092.
[10] K. Nadaoka, T. Kondoh, Laboratory measurements of velocity field structure in the surf zone by ldv, Coastal Eng. J. Japan 25 (1982) 125–145.
[11] E. Lamarre, W.K. Melville, Air entrainment and dissipation in breaking waves, Nature 351 (1991) 469.
[12] H.H. Hwung, J.M. Chyan, Y.C. Chung, Energy dissipation and air bubbles mixing inside surf zone, in: Proc. 23rd Intl Conf. on Coastal Eng., 1992, pp. 308–321.
[13] H. Chanson, S. Aoki, M. Maruyama, Unsteady air bubble entrainment and detrainment at a plunging breaker: dominant time scales and similarity of water level variations, Coastal Eng. 46 (2002) 139–157.
[14] C. Lin, H.H. Hwung, External and internal flow fields of plunging breakers, Exp. Fluids 12 (1992) 229–237.
[15] H. Chanson, J.-F. Lee, Plunging jet characteristics of plunging breakers, Coastal Eng. 31 (1997) 125–141.
[16] Z.-C. Huang, S.-C. Hsiao, H.-H. Hwung, K.-A. Chang, Turbulence and energy dissipations of surf-zone spilling breakers, Coastal Eng. 56 (2009) 733–746.
[17] S.F. Bradford, Progress in the observation and modeling of turbulent multi-phase flows, Environ. Fluid Mech. 9 (2) (2009) 121–123.
[18] E.D. Christensen, D.-J. Walstra, N. Emerat, Vertical variation of the flow across the surf zone, Coastal Eng. 45 (2002) 169–198.
[19] P.D. Hieu, K. Tanimoto, V.T. Ca, Verification of a vof-based two-phase flow model for wave breaking and wave-structure interactions, Ocean Eng. 33 (2006) 1565–1588.
[20] P. Lubin, S. Vincent, S. Abadie, J.-P. Caltagirone, Three-dimensional large eddy simulation of air entrainment under plunging breaking waves, Coastal Eng. 53 (2006) 631–655.
[21] Z. Wang, J. Yang, B. Koo, F. Stern, A coupled level set and volume-of-fluid method for sharp interface simulation of plunging breaking waves, Int. J. Multiph. Flow 35 (3) (2009) 227–246.
[22] Z. Wang, Q. Zou, D. Reeve, Simulation of spilling breaking waves using a two phase flow cfd model, Comput. Fluids 38 (10) (2009) 1995–2005.
[23] A. Iafrati, Numerical study of the effects of the breaking intensity on wave breaking flows, J. Fluid Mech. 622 (2009) 371–411.
[24] O. Kimmoun, H. Branger, A piv investigation on laboratory surf-zone breaking waves over a sloping beach, J. Fluid Mech. 588 (2007) 353–397.
[25] P. Lubin, H. Branger, O. Kimmoun, Large eddy simulation of regular waves breaking over a sloping beach, in: J.M. Smith (Ed.), Proceedings of the 30st International Conference on Coastal Engineering, Vol. 1, World Scientific, 2006, pp. 238–250. doi:10.1142/9789812709554_0021.
[26] O. Kimmoun, H. Branger, B. Zucchini, Laboratory piv measurements of wave breaking on a beach, in: Proc. 14th Int. Offshore and Polar Engng. Conf., Vol. 3, 2004, pp. 293–298.
[27] I. Kataoka, Local instant formulation of two-phase flow, Int. J. Multiphase Flow 12 (5) (1986) 745–758.
[28] E. Arquis, J.-P. Caltagirone, Sur les conditions hydrodynamiques au voisinage d'une interface milieu fluide - milieu poreux: application à la convection naturelle, C. R. Acad. Sci. Sér. II B 299 (1984) 1–4.
[29] P. Angot, C. Bruneau, P. Fabrie, A penalization method to take into account obstacles in incompressible viscous flows, Nümer. Math. 81 (4) (1999) 497–520.
[30] K. Khadra, P. Angot, S. Parneix, J.-P. Caltagirone, Fictitious domain approach for numerical modelling of Navier-Stokes equations, Internat. J. Numer. Methods Fluids 34 (2000) 651–684.
[31] P. Lubin, J.-P. Caltagirone, Large eddy simulation of the hydrodynamics generated by breaking waves, in: Q. Ma (Ed.), Advances in numerical simulation of nonlinear water waves, in: Advances in Coastal and Ocean Engineering, vol. 11, World Scientific Publishing Company, 2010, pp. 575–604. Ch. 16.
[32] P. Sagaut, Large Eddy Simulation for Incompressible Flows — An Introduction, Springer Verlag, 1998.
[33] P. Lubin, Large eddy simulation of plunging breaking waves, Ph.D. thesis, Université Bordeaux I (2004) (in English).
[34] P. Helluy, F. Gollay, S.T. Grilli, N. Seguin, P. Lubin, J.-P. Caltagirone, S. Vincent, D. Drevard, R. Marcer, Numerical simulations of wave breaking, Math. Model. Numer. Anal. 39 (3) (2005) 591–608.
[35] P. Lubin, S. Glockner, H. Chanson, Numerical simulation of a weak breaking tidal bore, Mech. Res. Commun. 37 (1) (2010) 119–121.
[36] P. Lubin, H. Chanson, S. Glockner, Large eddy simulation of turbulence generated by a weak breaking tidal bore, Environ. Fluid Mech. 10 (5) (2010) 587–602.
[37] P. Sagaut, R. Grohens, Discrete filters for large eddy simulation, Internat. J. Numer. Methods Fluids 31 (1999) 1195–1220.
[38] M. Rudman, A volume-tracking method for incompressible multifluid flows with large density variations, Internat. J. Numer. Methods Fluids 28 (2) (1998) 357–378.
[39] M. Fortin, R. Glowinski, Méthodes de lagrangien augmenté. Application à la résolution numérique de problèmes aux limites, Dunod, Paris, 1982.
[40] H. Uzawa, Iterative method for concave programming, in: K.J. Arrow, L. Hurwicz, H. Uzawa (Eds.), Studies in linear and Nonlinear Programming, Stanford University Press, Stanford, CA, 1958.
[41] S. Vincent, J.-P. Caltagirone, P. Lubin, T.N. Randrianarivelo, An adaptative augmented lagrangian method for three-dimensional multi-material flows, Comput. Fluids 33 (2004) 1273–1289.
[42] S.V. Patankar, Numerical Heat Transfer and Fluid Flow, Hemisphere Publishing Corporation, New York, 1990.
[43] P.R. Amestoy, I.S. Duff, J. Koster, J.-Y. L'Excellent, A fully asynchronous multifrontal solver using distributed dynamic scheduling, SIAM J. Matrix Anal. Appl. 23 (1) (2001) 15–41.
[44] P.R. Amestoy, A. Guermouche, J.-Y. L'Excellent, S. Pralet, Hybrid scheduling for the parallel solution of linear systems, Parallel Comput. 32 (2) (2006) 136–156.
[45] P. Lin, P.L.-F. Liu, Free surface tracking methods and their applications to wave hydrodynamics, in: Advances in Coastal and Ocean Eng., vol. 5, World Scientific, 1999, pp. 213–240.
[46] R.J. LeVeque, Numerical Methods for Conservation Laws, in: Lectures in Mathematics, Birkhauser, Zurich, 1992.
[47] P. Lubin, S. Vincent, J.-P. Caltagirone, On the Navier–Stokes equations simulation of the head-on collision between two surface solitary waves, C. R. Mécanique 333 (4) (2005) 351–357.
[48] P. Lin, P.L.-F. Liu, Internal wave-maker for Navier–Stokes equations models, J. Waterway Port Coastal Ocean Eng. 125 (4) (1999) 207–215.
[49] T. Yasuda, H. Mutsuda, N. Mizutani, Kinematics of overturning solitary waves and their relations to breaker types, Coastal Eng. 29 (1997) 317–346.
[50] J.-J. Lee, J.E. Skjelbreia, F. Raichlen, Measurements of velocities in solitary waves, J. Waterway Port Coastal Ocean Eng. WW2 108 (1982) 200–218.
[51] P. Lubin, H. Lemonnier, Propagation of solitary waves in constant depths over horizontal beds, Multiphase Sci. Technol. 16 (1–3) (2004) 237–248. doi:10.1615/MultScienTechn.v16.i1-3.310.
[52] F.J. Seabra-Santos, D.P. Renouard, A.M. Temperville, Numerical and experimental study of the transformation of a solitary wave over a shelf or isolated obstacle, J. Fluid Mech. 176 (1997) 117–134.
[53] P.L.-F. Liu, Y. Cheng, A numerical study of the evolution of a solitary wave over a shelf, Phys. Fluids 13 (6) (2001) 1660–1667.
[54] G. Chen, C. Kharif, S. Zaleski, J.J. Li, Two-dimensional Navier–Stokes simulation of breaking waves, Phys. Fluids 11 (1999) 121–133.
[55] J.D. Fenton, A fifth-order stokes theory for steady waves, J. Waterway Port Coastal Ocean Eng. 111 (1985) 216–234.
[56] D.H. Peregrine, Breaking waves on beaches, Annu. Rev. Fluid Mech. 15 (1983) 149–178.
[57] R.J. Sobey, P. Goodwin, R.J. Thieke, R.J. Westberg, Application of stokes, conoidal, and fourier wave theories, J. Waterway Port Coastal Ocean Eng. 113 (6) (1987) 565–587.
[58] J.D. Fenton, W.D. McKee, On calculating the lengths of water waves, 14 (1990) 499–513.
[59] J.H. Duncan, Spilling breakers, Annu. Rev. Fluid Mech. 33 (2001) 519–547.
[60] P. Bonmarin, Geometric properties of deep-water breaking waves, J. Fluid Mech. 209 (1989) 405–433.
[61] T. Sakai, T. Mizutani, H. Tanaka, Y. Tada, Vortex formation in plunging breaker, in: Proc. ICCE, 1986, pp. 711–723.
[62] G.B. Deane, M.D. Stokes, Scale dependence of bubble creation mechanisms in breaking waves, Nature 418 (2002) 839–844.
[63] F.C.K. Ting, J.T. Kirby, Observation of undertow and turbulence in a laboratory surf zone, Coastal Eng. 24 (1994) 51–80.
[64] F.C.K. Ting, J.T. Kirby, Dynamics of surf-zone turbulence in a strong plunging breaker, Coastal Eng. 24 (1995) 177–204.
[65] F.C.K. Ting, J.T. Kirby, Dynamics of surf-zone turbulence in a spilling breaker, Coastal Eng. 27 (1996) 131–160.

[66] P. Lin, P.L.-F. Liu, A numerical study of breaking waves in the surf zone, J. Fluid Mech. 359 (1998) 239–264.
[67] P. Lin, P.L.-F. Liu, Discussion of vertical variation of the flow across the surf zone, Coastal Eng. 50 (3) (2004) 161–164.
[68] K. Nadaoka, M. Hino, Y. Koyano, Structure of the turbulent flow field under breaking waves in the surf zone, J. Fluid Mech. 204 (1989) 359–387.
[69] F. Shi, J.T. Kirby, G. Ma, Modeling quiescent phase transport of air bubbles induced by breaking waves, Ocean Modelling 35 (1–2) (2010) 105–117.